Superconductor Science and Technology

LETTER

Rapid Nb_3Sn film growth by sputtering Nb on hot bronze

To cite this article: Wenura K Withanage *et al* 2021 *Supercond. Sci. Technol.* **34** 06LT01

IOP Publishing

Letters

Superconductor Science and Technology

Supercond. Sci. Technol. **34** (2021) 06LT01 (7pp)

https://doi.org/10.1088/1361-6668/abf66f

Letter

Rapid Nb_3Sn film growth by sputtering Nb on hot bronze

Wenura K Withanage[1,*], Andre Juliao[1,2] and Lance D Cooley[1,3]

[1] Applied Superconductivity Center, National High Magnetic Field Laboratory, Tallahassee, FL 32310, United States of America
[2] Department of Physics, Florida State University, Tallahassee, FL 32306, United States of America
[3] College of Engineering, Florida State University and Florida A&M University, Tallahassee, FL 32310, United States of America

E-mail: withanage@asc.magnet.fsu.edu

Received 21 January 2021, revised 27 March 2021
Accepted for publication 9 April 2021
Published 4 May 2021

Abstract

Nb deposited by magnetron sputtering onto hot Cu-15 wt.%Sn bronze substrates at temperatures above 700 °C achieved Nb_3Sn film growth at a rate of 33 nm min^{-1}, which was an order of magnitude faster than that achieved for deposition of Nb on bronze at low temperature followed by *in situ* post reaction at the same high temperatures. Tin content in the Nb_3Sn films made on hot bronze was ∼26.3%, which is significantly higher than ∼24.5% obtained by post-reaction as well as for typical bulk reactions between Nb and α-bronze. The Nb_3Sn lattice parameter was consistent with measured tin content and predicted elastic strain for both routes. Critical temperatures of 14 K–16 K, instead of 18 K, were consistent with elastic strain due to coefficient of thermal expansion mismatch between the Nb_3Sn and bronze substrate and, for the hot-bronze samples, stress related to the growth mechanism. Films were fully coalesced and had surface roughness values <20 nm over a 100 μm^2 scan. Grain structure of the Nb_3Sn films produced by Nb sputtering on hot bronze resembles zone 2 in the Thornton structure-zone diagram, in contrast to the equiaxed grain structure reminiscent of microstructure observed in reacted Nb_3Sn wires exhibited by the post-reaction route.

Keywords: Nb_3Sn, superconducting radio frequency cavities, SRF, thin films, bronze route

(Some figures may appear in colour only in the online journal)

1. Introduction

Development of Nb_3Sn films for superconducting radio-frequency (SRF) cavities has received recent attention in view of their potential to operate using a cryocooler at 4 K–8 K, in contrast to conventional Nb cavity operation using superfluid helium at ∼2 K [1, 2]. Nb_3Sn has a critical temperature T_c of 18.3 K, double the T_c of Nb, and this gives a fundamental advantage to the cavity quality factor Q and related RF losses. Continuous-wave operation of conduction-cooled Nb_3Sn cavities has been demonstrated recently [3–5], and for many applications at <10 MV m^{-1} [6] a very compact electron accelerator may be possible [7]. Nb_3Sn also has a thermodynamic critical field (extrapolated to 0 K) of 540 mT, which is double that of Nb. Along with Q, critical field is a principal contributor to the theoretical limit of accelerating gradient E_{ac}.

Research and development of Nb_3Sn cavity coatings has been primarily focused on the vapour diffusion technique, where a bulk Nb cavity is reacted with Sn vapour at ∼1100 °C to achieve stoichiometric Nb_3Sn via binary reaction while avoiding formation of other Nb–Sn phases [2, 8–10]. Since this is above the melting point of Cu and Al, adding these metals to facilitate conduction cooling requires a post-process [3, 4].

* Author to whom any correspondence should be addressed.

Control of growth requires a careful balance of tin vapour pressure, wetting and adsorption of Sn on the Nb_3Sn surface, net flux of tin atoms entering and leaving the Nb_3Sn surface, diffusion of Sn through the Nb_3Sn layer, and reaction rate at the Nb–Nb_3Sn interface [9, 11–15].

Forming Nb_3Sn at temperatures compatible with a Cu cavity template is an alternative to the Sn vapour approach above. Formation of Nb_3Sn *in situ* at temperatures compatible with Cu has been demonstrated by sputtering from a composite target [16, 17], co-sputtering Nb and Sn [18], by reaction of sequential Nb and Sn layers [19], and by reaction of deposited Nb with bronze [20, 21]. Room-temperature electrodeposition of Nb and Sn or bronze layers followed by a post-process reaction also shows promise [22]. Reactions using bronze can avoid unwanted Nb_6Sn_5 and $NbSn_2$ at 600 °C–800 °C and adapt from techniques used for wire conductors [23, 24]. Chemical vapour deposition generally requires temperatures at the limit of Cu compatibility to achieve useful vapour pressure of reactants [11], although new techniques [25] appear promising.

However, physical deposition processes must overcome low atomic mobility to attain film coalescence and avoid structural defects [26]. The fact that the melting point of copper, 1358 K, is significantly below that of Nb_3Sn, ∼2385 K [24], means that substrate heating has limited benefit during deposition, and long post-deposition annealing times may be needed to fill in pinholes and channels, reduce stress, and relax needle-like columnar grain structures [16, 17]. During this process, Sn could be lost as vapour or diffusion into the Cu base, resulting in a tin-poor Nb_3Sn layer [9]. For bronze methods, challenges exist for supplying high tin activity and possible Cu contamination in grain boundaries. Expansion of Nb by 37% upon conversion to Nb_3Sn could pose additional challenges for solid-state reactions. Another issue for Nb_3Sn films is the significant difference between the coefficients of thermal expansion (CTE) of Nb_3Sn and Cu, which places any Nb_3Sn coating on Cu under compression when cooled, and reduces T_c from ∼18 K to ∼15 K.

In this paper, we report rapid Nb_3Sn film synthesis from deposition of Nb onto hot bronze. We observe nanostructure unlike those produced by any of the methods compatible with Cu above. The Nb_3Sn film showed columnar grain growth which resembles the structure zone 2 in Thornton structure zone diagram [27, 28]. Moreover, Nb_3Sn coatings with Sn content ∼26.3% were achieved at 715 °C, suggesting tin activity is high. For comparison, we also report Nb_3Sn films created by post-reaction after depositing Nb at low temperature and then heating in the film chamber for 6 h at ∼650 °C–715 °C to produce the diffusion reaction. These films attained slightly lower tin content ∼24.5% Sn, and they did not exhibit similar columnar grain growth suggesting equiaxed grain growth characteristic of reactions in wires [29]. Growth was an order of magnitude faster for the hot bronze route, achieving 0.7 μm thickness in 22 min, compared to 360 min or more required for the post-deposition reaction. While bronze methods have challenges, there could be significant advantages for material cost, cavity fabrication, and compatibility with Cu.

2. Experimental details

Mirror polished zero-phosphorus Cu-15 wt.%Sn bronze pieces were used as substrates in this experiment. Typical substrate dimensions were around ∼7.5 mm × ∼7.5 to 15 mm × ∼1 mm. The composition was chosen to be close to the highest Sn solubility in α-bronze, since high Sn activity is necessary to produce stoichiometric Nb_3Sn [24]. Nb was deposited by DC magnetron sputtering at 250 W using 8 mTorr Ar gas, which yielded 0.374 nm s^{-1} deposition rate as calibrated by a quartz oscillator for room-temperature deposition. Typical background pressure was ∼5 × 10^{-9} Torr. All synthesis occurred *in situ*, using a radiant substrate heater with a thermocouple attached to the substrate heater assembly. The actual substrate temperature is below the deposition temperature setpoints (∼60 °C below at 775 °C), and temperatures reported here account for measured differences. For deposition on hot bronze, substrates were pre-heated for 1 h before Nb deposition and concurrent Nb_3Sn reaction. Temperature was maintained during deposition of 0.5 μm Nb, resulting in 0.7 μm thick Nb_3Sn. At the end of the Nb deposition, the substrate heater was turned off. Post-reacted films were prepared by first depositing the same thickness of Nb at 200 °C, then ramping the substrate heater up to >600 °C under high-vacuum conditions. Maximum heat treatment length was limited to 6 h by deposition chamber hardware. Films of Nb deposited on bronze at 200 °C but not given a post-reaction treatment produced the expected Nb structure and T_c = 9.2 K with very sharp transition.

Measurements of magnetic moment m vs temperature T used a SQUID magnetometer (Quantum Design MPMS) to determine the T_c of the films. Samples were cooled in zero field and then 1 mT field was applied perpendicular to the film. A Rigaku SmartLab system was used for x-ray diffraction (XRD). A FEI Helios G4 UC field emission scanning electron microscope (SEM) was used to study the surface morphologies in secondary electron (SE) mode and the elemental composition of the samples in energy dispersive spectroscopy (EDS) using an Oxford Instruments X-Max^N SDD x-ray detector and standard-less analysis. Roughness of the substrates and the films were measured using a Veeco Icon atomic force microscope.

In the discussion below, we describe Nb_3Sn films made by depositing 500 nm Nb layer on hot bronze at 650 °C and 715 °C, which henceforth are identified as H1 and H2, respectively. We also compare Nb_3Sn samples made by post reacting a 500 nm Nb film at 650 °C and 715 °C with 6 h heat treatments, which henceforth are identified as PR1 and PR2 respectively. Table 1 summarizes the details of the growth process and some of the properties observed in these samples.

3. Results

3.1. XRD analysis

XRD measurements show multiple peaks according to the known sequence for Nb_3Sn crystal planes. Figure 1 shows the

Table 1. Summary of sample preparation details and properties.

Sample ID	Growth method	Growth/reaction temperature	Growth/reaction time	T_c-onset	Sn content	Strain
H1	Hot-bronze	∼650 °C	22 min	∼8.8 K, ∼13 K	Not fully reacted	–1.14%
H2	Hot-bronze	∼715 °C	22 min	∼14.5 K	∼26.3%	–1.24%
PR1	Post-reaction	∼650 °C	360 min	∼9.2 K, ∼13 K	Not fully reacted	–0.92%
PR2	Post-reaction	∼715 °C	360 min	∼14.5 K	∼24.5%	–0.88%

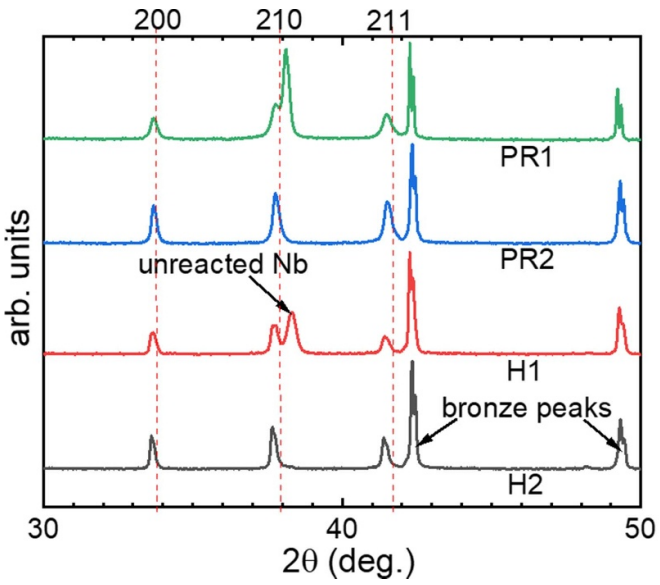

Figure 1. X-ray diffraction patterns for the Nb_3Sn coatings studied.

principal peaks for H1, H2, PR1, and PR2. Both routes produced polycrystalline Nb_3Sn films based on the lack of indications consistent with preferred growth. Complete conversion of Nb to Nb_3Sn is evident for the higher temperature reaction. Nb_3Sn lattice parameter perpendicular to the film was determined using the position of multiple peaks and averaged. Slight expansion in the out-of-plane lattice parameter was observed in comparison to the stoichiometric Nb_3Sn value of 5.290 Å [24], possibly indicating an in-plane compressive strain. Measured out-of-plane lattice parameters of the 715 °C hot bronze and post-reacted samples are 5.336 Å and 5.323 Å, respectively. Using Nb_3Sn Poisson's ratio of 0.35 [30], in-plane strain of −1.24% and −0.88% respectively for the hot bronze and the post-reacted film can be estimated. The latter value is consistent with the CTE mismatch between Nb_3Sn and bronze for cooling from 715 °C to 25 °C [31].

3.2. Microstructure and elemental analysis

Figures 2 and 3 show SEM surface and cross-section images of the H2 and PR2 samples. Features of the underlying bronze microstructure are evident in the low-magnification images. A distinct wavy surface feature correlates with the location of bronze grain boundaries for the hot-bronze sample, figure 2(a). In figure 2(b), Nb_3Sn grains have somewhat larger size at wavy grain-boundary regions, which may be related to high tin content in the underlying bronze as will be discussed later. Smooth Nb_3Sn covers the interior of bronze grains for the hot-bronze sample, figure 2(c), as well as uniformly covering the post-reacted sample, figures 2(d) and (e). Figure 2(e) shows many grain facets tilted from the film plane, while figures 2(b) and (c) are dominated by facets lying close to the film plane. Post-reaction produces the smallest grain size. Average roughness (R_a) of the hot bronze and post-reacted samples were 7–15 nm taken over several 100 μm^2 scans within the interior of underlying bronze grains.

Cross-section SEM images are compared in figure 3. The final Nb_3Sn layer thickness is ∼725 nm for the hot bronze specimen reacted at 715 °C, which corresponds to a ∼44% increase in thickness with respect to the Nb layer. The thickness of the post-reacted Nb_3Sn layer is ∼640 nm, which is ∼28% increase in thickness. Contrast blocks in figure 3(a) suggest that columnar Nb_3Sn grains span the entire film thickness in the hot-bronze sample, which is zone 2 in Thornton thin-film structure zones [27, 28]. The width of the columnar Nb_3Sn grains is several hundred nanometres if each contrast block is one grain. By comparison, contrast blocks in figure 3(b) have much smaller size and do not have consistent arrangement with respect to the film plane. The contrast is suggestive of smaller equiaxed grains as observed in bronze route Nb_3Sn wires [29]. Large grains also occur at the interface between bronze and the Nb_3Sn layer in post-reacted samples, figure 3(b), and these grains grow into the bronze. EDS indicates that this is a Cu–Sn–Nb compound like that found in some Nb_3Sn wires [32, 33]. Cracks are not evident in surface or cross-section images.

Spectroscopy results using a 7 keV electron beam give Sn content in the hot bronze films ∼26.3% and slightly lower Sn content, ∼24.5% in the post-reacted samples. Figures 4(a) and (b) show line scans across the Nb_3Sn layer of H2 and PR2 respectively. While artefacts exist near the edges of Nb_3Sn layer, flat Nb and Sn amplitude in the central region of both scans. Slightly higher Cu content was observed in the central scan region of PR2, ∼3.3% compared to ∼0.9% for H2.

3.3. Superconducting transition temperature measurements

Figure 5(a) compares T_c measurements of H1, H2, PR1, and PR2. The transitions at 12 K–15 K are due to the Nb_3Sn phase, while the partial transitions at ∼9 K are due to unreacted Nb due to the low Sn activity at ∼650 °C. For 715 °C, the single transition indicates the full conversion of Nb to Nb_3Sn. Figure 4(b) shows the m vs T curves near the transition onset, where the data curves for the hot-bronze samples have crossed those of the post-reaction samples. The transitions are fairly

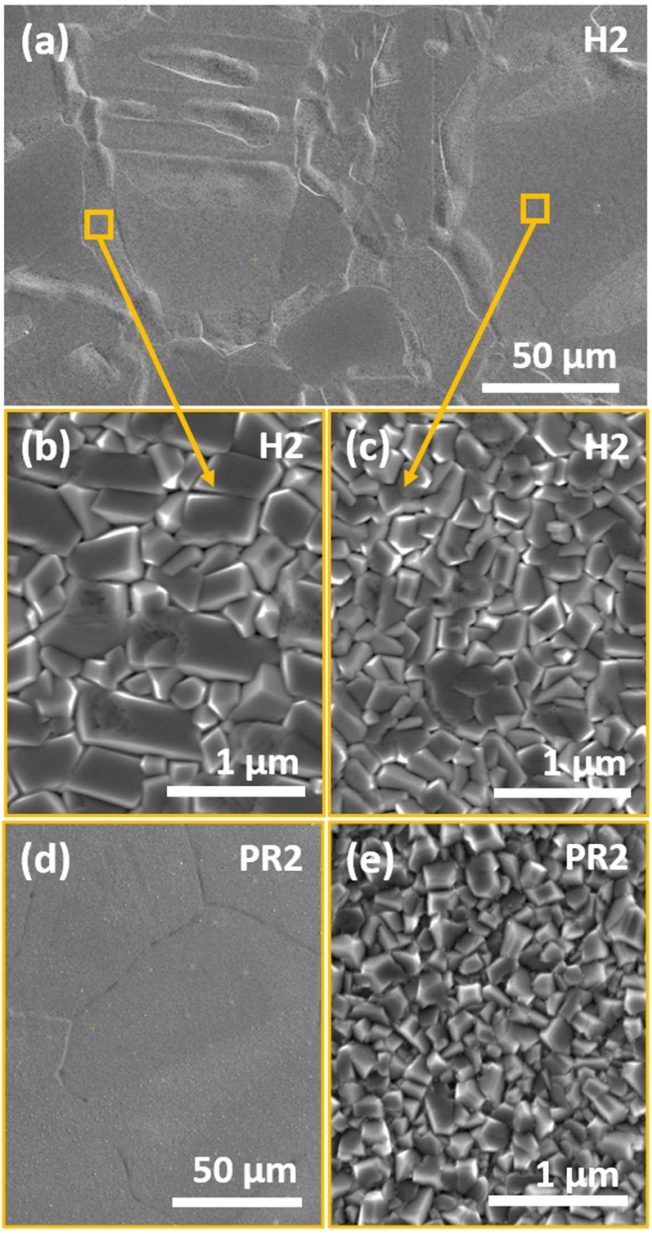

Figure 2. SEM-SE images of a Nb_3Sn film deposited on hot bronze is shown in (a)–(c) at different scales. The yellow boxes in (a) show the general area from where images (b) and (c) are taken. Images (d) and (e) show a Nb_3Sn film made by the corresponding post-reaction method.

broad, with the midpoint of the Nb_3Sn region being ∼2 K below the onset.

4. Discussion

This report compares specific samples from a larger study [34] to explicitly compare Nb_3Sn film synthesis using the hot bronze and the post-reaction approaches. Significantly, different growth rate and microstructure resulted, yet the samples had comparable superconducting properties. In the hot-bronze approach, 725 nm Nb_3Sn with ∼26.3% Sn content formed in just 22 min at 715 °C. By contrast, the post-reaction method at

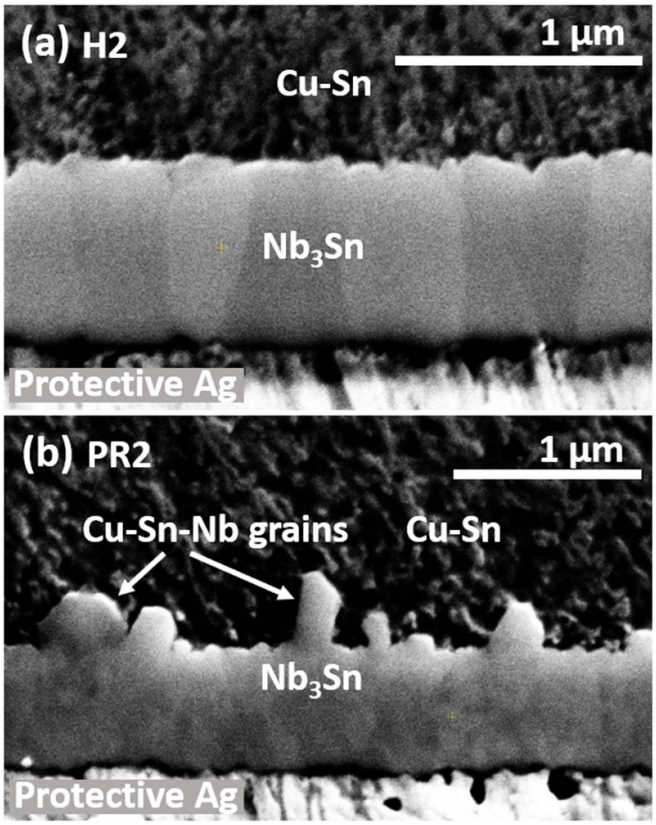

Figure 3. SEM-SE images of cross-sections of Nb_3Sn films made at 715 °C by deposition of Nb on hot bronze (a) and via post-reaction (b).

the same temperature required 360 min to produce a 640 nm Nb_3Sn layer with ∼24.5% Sn. Higher tin content produces better superconducting properties [24], and it is rather surprising to obtain stoichiometric Nb_3Sn via a bronze reaction at these temperatures. Usually internal-tin routes [23, 24], which have more available tin, are needed to approach stoichiometry, yet doing so only for long reactions well above 650 °C.

The columnar grain structure seen in the hot-bronze films, figure 3(a), is different from that observed in the post-reacted films, figure 3(b). It is also an unusual microstructure based on observations of Nb_3Sn wires [23] for reactions in this temperature range and duration. On the other hand, the post-reaction films have microstructure consistent with observations in the literature for similar reaction temperature and time. In [35], layer growth rate for binary and alloyed Nb_3Sn was modelled via a power law $d = kt^n$ where d is the layer thickness, k is a constant, t is time, and n is related to the growth mechanism. For growth limited by grain-boundary diffusion of tin [35], reports $n = 0.33$ and finds $k = 26$ nm s^{-1} at 750 °C. These parameters predict a ∼700 nm layer in 6 h, which is roughly equivalent to the thickness shown in figure 3(b) for PR2. Reference [35] also identifies a change in the growth rate and microstructure to a condition limited by bulk diffusion of tin through Nb_3Sn at 800 °C, where notably the exponent n increases to 0.5 with $k = 11$ nm s^{-1} and large columnar grains are found. Inserting the H2 growth time of 22 min yields a layer growth of 400 nm, which is

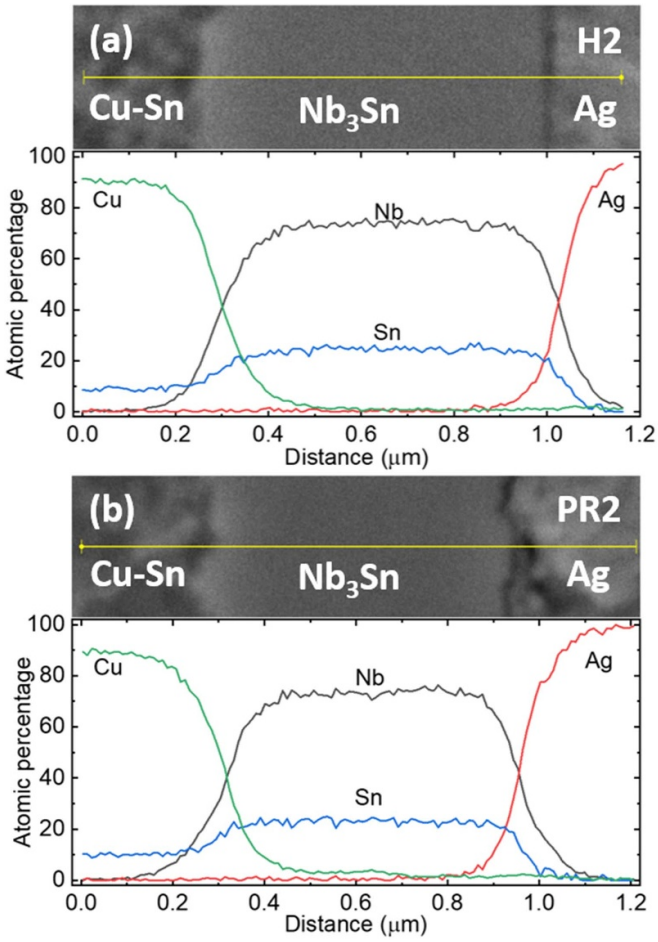

Figure 4. EDS line scans of cross-section images of (a) H2 and (b) PR2.

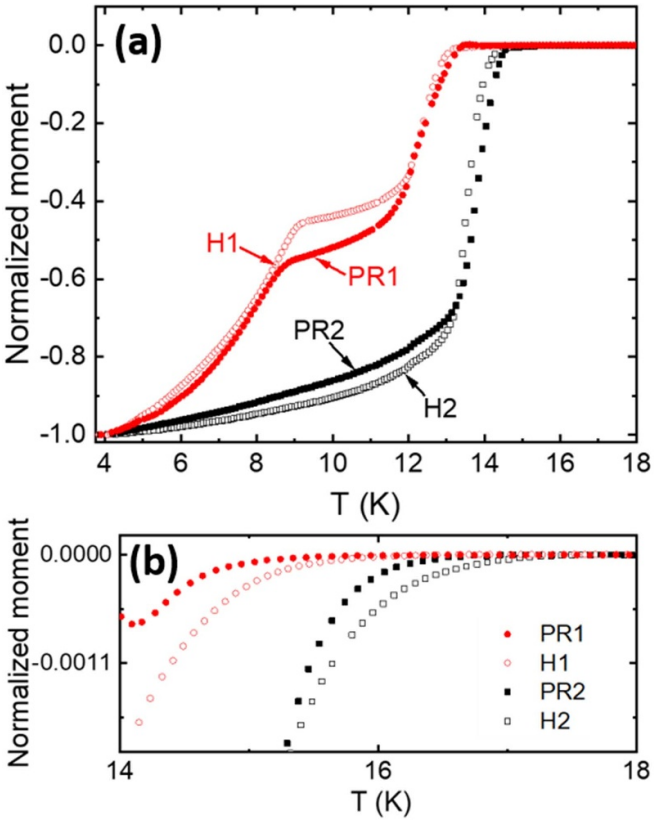

Figure 5. (a) T_c measurements of samples made at 650 °C and 715 °C. (b) The onset of the T_c transitions.

somewhat less than that observed in figure 3(a). So, while high-rate planar growth might describe the unusual microstructure of the hot bronze samples, there appears to be additional rate enhancement for films, as discussed below. When 1 μm Nb layer was deposited on hot bronze, evidence for unreacted Nb was observed in T_c and XRD measurements, which indicates that Sn arrival to the growth front slows down as the Nb_3Sn layer thickness increases [34]. However, thicker Nb_3Sn films may be possible with slower Nb deposition rates.

Unusually high tin activity may be present at the hot bronze surface to further facilitate rapid formation of Nb_3Sn with high Sn content. During pre-heating of bronze in high vacuum, the surface takes on a silvery colour, which is consistent with diffusion of Sn atoms to the bronze surface to maintain thermodynamic vapour pressure. This Sn-rich surface layer would supply high Sn activity for arriving Nb atoms. Under these conditions, nucleation of Nb_3Sn islands can occur at a high rate. High Sn mobility would subsequently facilitate coalescence and rapid growth of columnar grains as additional Nb atoms arrive. The flat facets at the surface in figures 2(b) and (c) and the columnar grain structure in figure 3(a) are distinguishing features of zone 2 in the Thornton structure zones [27, 28].

Coalescence of grains and healing of defects are important for crack-free dense Nb_3Sn coatings, and these critical processes appear to be facilitated by deposition of Nb onto hot bronze. This should be advantageous for SRF applications. The coalescence process is consistent with the Volmer–Weber mechanism. The fact that the columns are 200–500 nm wide indicates high mobility and possible recrystallization, in contrast to when mobility is low and columns have width characteristic of the nucleus size, 20–50 nm [26].

Moreover, connecting the XRD, T_c and EDS data requires details consistent with high-mobility Volmer–Weber growth. Post-reaction samples should not have significant intrinsic strain, based on results for composite wires [24], so we attribute the PR T_c data as being solely determined by the tin composition and the CTE mismatch strain. The lattice parameter differences indicated by XRD suggest that H films have intrinsic compression in addition to CTE mismatch compared to the PR films. The extra strain explains why H and PR films exhibit similar T_c values despite the H samples being higher in Sn content. The origin of compressive intrinsic stress in the H films could be due to the high-mobility Volmer–Weber mechanism [26, 36–38].

The morphology change above bronze grain boundaries in figure 2(a) and the Nb–Cu–Sn phase in figure 3(b) may be artefacts of the behaviour of bronze in vacuum. According to the Cu-Sn phase diagram [39], any local deviations above 15% weight Sn bronze will become mixed phase, α and β, above

518 °C. Despite our achievement of homogeneous bronze, it is plausible that extraction of Sn vapour under vacuum could encourage Sn diffusion to grain boundaries while the substrate warms. From EDS of uncoated bronze substrates heated to 715 °C and then cooled in vacuum, it was discovered that the wavy grain-boundary regions in figure 2(a) are above Cu ∼ 33 wt.%Sn, i.e. γ phase, while large smooth bronze grains contained ∼16 wt.%Sn. Lower Sn content, 13 wt.%, could suppress this artefact, at the risk of reducing tin activity and altering the growth mode.

5. Conclusion

In this work, we described rapid Nb_3Sn film growth when Nb was deposited on hot bronze, producing an immediate conversion to Nb_3Sn. This mechanism is not available to solid-state reactions. A factor of 12 faster growth rate for ∼700 nm thick films was observed, in comparison to deposition of Nb onto bronze at 200 °C (where no reaction occurs) followed by a post-reaction at the same temperature. The hot-bronze Nb_3Sn films had a columnar grain structure similar to Thornton structure zone 2, whereas the post-reaction method produced smaller equiaxed grains characteristic of reactions in wires. Samples showed smooth Nb_3Sn surface with no cracks, and high tin content. Critical temperature was consistent with tin content and strain, with significant reduction to 14 K–16 K from the ∼18 K of bulk stoichiometric Nb_3Sn due to the strain induced by CTE mismatch between Nb_3Sn and bronze. The hot-bronze approach can be scaled to applications such as SRF cavities and devices as it produces smooth, dense, crack-free, and stoichiometric Nb_3Sn coatings with relatively easy process.

Data availability statement

The data that support the findings of this study are available upon reasonable request from the authors.

Acknowledgments

Authors would like to thank Peter J Lee (ASC-NHMFL), Shreyas Balachandran (ASC-NHMFL), Choong-Un Kim (University of Texas—Arlington), and John Buttles (Bailey Tool & Mfg., Lancaster TX) for fruitful discussions. We also thank Shengzhi Zhang (NHMFL) and Wan Kyu Park (NHMFL) for proving Nb films on bronze substrates during preliminary studies. Preparation of bronze was completed at Ames Laboratory with further processing at Bailey Tool. Undergraduate students providing metallographic polishing include Christopher Reis, Jonathan Wozny, and Alexander Wozny. This work was supported by the U.S. Department of Energy, Office of Science, Office of High Energy Physics under Award No. DE-SC 0018379. A portion of this work was performed at the National High Magnetic Field Laboratory, which is supported by National Science Foundation Cooperative Agreement No. DMR-1644779 and the State of Florida.

ORCID iDs

Wenura K Withanage https://orcid.org/0000-0003-1350-9423
Lance D Cooley https://orcid.org/0000-0003-3488-2980

References

[1] Valente-Feliciano A-M 2016 *Supercond. Sci. Technol.* **29** 113002
[2] Posen S and Hall D L 2017 *Supercond. Sci. Technol.* **30** 033004
[3] Dhuley R C, Posen S, Geelhoed M I, Prokofiev O and Thangaraj J C T 2020 *Supercond. Sci. Technol.* **33** 06LT01
[4] Ciovati G, Cheng G, Pudasaini U and Rimmer R A 2020 *Supercond. Sci. Technol.* **33** 07LT01
[5] Stilin N, Holic A, Liepe M, Porter R and Stable S J 2020 (arXiv:200211755) [physics]
[6] 2015 Report of the DOE basic research needs workshop on energy & environmental applications of accelerators (available at: www.acceleratorsamerica.org/workshops/index.html)
[7] Kephart R *et al* 2015 *Proc. SRF2015* (*Whistler, BC, Canada*)
[8] Heinrichs H, Arnolds-Mayer G, Grundey T, Klein U, Minatti N, Müller G, Peiniger M, Piel H, Unterborsch G and Vogel H P 1984 *Proc. 2nd Workshop on RF Superconductivity* (*Geneva*)
[9] Pudasaini U, Eremeev G, Reece C E, Ciovati G, Parajuli I, Sayeed N and Kelley M J 2019 *Proc. SRF2019* (*Dresden, Germany*)
[10] Porter R, Arias T, Cueva P, Hall D L, Liepe M, Maniscalco J T, Muller D A and Sitaraman N 2018 *Proc. LINAC2018* (*Beijing, China*)
[11] Hanak J J, Strater K and Cullen G W 1964 *RCA Rev.* **25** 342
[12] Eremeev G, Clemens W, Macha K, Reece C E, Valente-Feliciano A M, Williams S, Pudasaini U and Kelley M 2020 *Rev. Sci. Instrum.* **91** 073911
[13] Pudasaini U, Eremeev G V, Reece C E, Tuggle J and Kelley M J 2020 *Supercond. Sci. Technol.* **33** 045012
[14] Trenikhina Y, Posen S, Romanenko A, Sardela M, Zuo J M, Hall D L and Liepe M 2018 *Supercond. Sci. Technol.* **31** 015004
[15] Becker C, Posen S, Groll N, Cook R, Schlepütz C M, Hall D L, Liepe M, Pellin M, Zasadzinski J and Proslier T 2015 *Appl. Phys. Lett.* **106** 082602
[16] Wu C T, Kampwirth R T and Hafstrom J W 1977 *J. Vac. Sci. Technol.* **14** 134–7
[17] Ilyina E A, Rosaz G, Descarrega J B, Vollenberg W, Lunt A J G, Leaux F, Calatroni S, Venturini-Delsolaro W and Taborelli M 2019 *Supercond. Sci. Technol.* **32** 035002
[18] Schäfer N, Karabas N, Palakkal J P, Petzold S, Major M, Pietralla N and Alff L 2020 *J. Appl. Phys.* **128** 133902
[19] Sayeed M N, Pudasaini U, Reece C E, Eremeev G and Elsayed-Ali H E 2019 *J. Alloys Compd.* **800** 272–8
[20] Hakimi M 1988 *J. Less-Common Met.* **139** 159–65
[21] Cooley L D and Lee P J 2001 *IEEE Trans. Appl. Supercond.* **11** 3820–3
[22] Barzi E, Bestetti M, Reginato F, Turrioni D and Franz S 2016 *Supercond. Sci. Technol.* **29** 015009
[23] Lee P J and Larbalestier D C 2008 *Cryogenics* **48** 283–92
[24] Godeke A 2006 *Supercond. Sci. Technol.* **19** R68
[25] Ge M, Arrieta V, Gruber T, Kaufman J, Liepe M, Maniscalco J, McNeal S, Oseroff T, Porter R and Sun Z 2019 *Proc. SRF2019* (*Dresden, Germany*)
[26] Koch R 1994 *J. Phys.: Condens. Matter* **6** 9519
[27] Thornton J A 1975 *J. Vac. Sci. Technol.* **12** 830
[28] Anders A 2010 *Thin Solid Films* **518** 4087–90

[29] Flükiger R, Uglietti D, Senatore C and Buta F 2008 *Cryogenics* **48** 293–307
[30] Poirier M, Plamondon R, Cheeke J D N and Bussière J F 1984 *J. Appl. Phys.* **55** 3327–32
[31] Easton D S, Kroeger D M, Specking W and Koch C C 1980 *J. Appl. Phys.* **51** 11
[32] Martin S, Walnsch A, Nolze G, Leineweber A, Léaux F and Scheuerlein C 2017 *Intermetallics* **80** 16–21
[33] Lachmann J, Huber N and Leineweber A 2020 *Mater. Charact.* **168** 110563
[34] Withanage W in preparation
[35] Osamura K, Ochiai S, Kondo S, Namatame M and Nosaki M 1986 *J. Mater. Sci.* **21** 1509–16
[36] Floro J A, Hearne S J, Hunter J A, Kotula P, Chason E, Seel S C and Thompson C V 2001 *J. Appl. Phys.* **89** 4886–97
[37] Tello J S, Bower A F, Chason E and Sheldon B W 2007 *Phys. Rev. Lett.* **98** 216104
[38] Yu H Z and Thompson C V 2014 *Acta Mater.* **67** 189–98
[39] Fürtauer S, Li D, Cupid D and Flandorfer H 2013 *Intermetallics* **34** 142–7